Hindawi
Journal of Nanomaterials
Volume 2019, Article ID 4257270, 9 pages
https://doi.org/10.1155/2019/4257270

Research Article

Synthesis and Photocatalytic Properties of Co-Doped $Zn_{1-x}Co_xMn_2O$ Hollow Nanospheres

Long Ma,[1,2] Zhiqiang Wei,[1,2] Xueliang Zhu,[2] Jiahao Liang,[2] and Xudong Zhang[2]

[1]*State Key Laboratory of Advanced Processing and Recycling of Non-Ferrous Metals, Lanzhou University of Technology, Lanzhou 730050, China*
[2]*School of Science, Lanzhou University of Technology, Lanzhou 730050, China*

Correspondence should be addressed to Zhiqiang Wei; qianweizuo@163.com

Received 20 December 2018; Accepted 21 March 2019; Published 9 May 2019

Guest Editor: Zhen Yu

A series of Co-doped $Zn_{1-x}Co_xMn_2O$ nanocrystals with a spinel structure were successfully prepared by hydrothermal method, and the influence of Co doping concentration on the microstructure, morphology, elemental composition, and optical and photocatalytic properties of the samples was characterized. The experimental results show that all samples exhibit a tetragonal structure, Co^{2+} ions are successfully substituted for the lattice site of Zn^{2+} to generate $ZnMn_2O_4$ nanocrystals, and the crystalline size decreases as Co-doped concentration increase. The morphologies are loose hollow microsphere structures. The band gap of $Zn_{1-x}Co_xMn_2O$ samples is smaller than that of pure $ZnMn_2O_4$ and has been red shifted. The photocatalytic activity of doped $Zn_{1-x}Co_xMn_2O_4$ samples is obviously higher than that of pure $ZnMn_2O_4$ samples for the photodegradation of MO under visible light irradiation. All these results demonstrate that Co-doped spinel $ZnMn_2O_4$ nanocrystals are a meaningful choice for photocatalytic degradation of the pollutants.

1. Introduction

In recent decades, with the development of modern industry, the growth of population, and the acceleration of urbanization, the increased pollution of natural water and air has become one of the major challenges that the modern human society and the ecological system are is facing and the main pollution sources are nondegradable and toxic artificial dyes [1–4]. The toxic compounds in water media cause serious harm to human health. Nanoscale semiconductor photocatalysts have attracted extensive research interest in the field of environmental restoration owing to their potential value, such as nontoxic, inexpensive, strong oxidizing activity, and chemical stability [5–8].

Spinel structure $ZnMn_2O_4$ belongs to I41/amd space group, and with a narrow band gap of 1.86 eV [9, 10]. $ZnMn_2O_4$ nanocrystals possess unique properties that are quite different from those of the bulk solid state due to their surface effect, quantum size effect, small size effect, and quantum tunnelling effect [11, 12]. Spinel structure $ZnMn_2O_4$ nanocrystals have attracted considerable attention due to their novel properties and broad application prospect in the gas sensor [13], photocatalyst [14], supercapacitor electrode [15, 16], lithium ion battery anode [17], energy storage [18], nonvolatile memory [19], etc. In recent years, some researchers have studied transition metal ion-doped $ZnMn_2O_4$ nanocrystals to obtain the desired crystal structure and energy band structure by providing extra positive carriers in the host material [20]. The crystal structure and energy band structure of semiconductor materials can be modified to improve their physical properties by controlling the preparation process, changing the type and amount of doped elements [21, 22]. In addition, transition metal ion configuration doping can significantly improve the separation rate of photoinduced carriers in semiconductor photocatalysts, inhibit the recombination of photoinduced electron hole pairs, and greatly improve photocatalytic activity [23]. Unfortunately, as far as we know, there are few reports about the influence of doping concentration on the photocatalytic performance of the transition

metal-ion doped ZnMn2O4 nanostructure. Therefore, the main purpose of this study is to study the effect of doping concentration on the microstructure and photocatalytic activity.

In this work, Co-doped $Zn_{1-x}Co_xMn_2O$ nanocrystals with different ratios ($x = 0$, 0.1, 0.3, and 0.5) were successfully synthesized by hydrothermal method. The influence of Co doping concentration on the microstructure, morphology, elemental composition, and optical properties of the samples was investigated by X-ray diffraction (XRD), field emission scanning electron microscopy (FESEM), X-ray energy dispersive spectrometry (XEDS), ultraviolet-visible spectroscopy (UV-Vis), and Fourier transform infrared spectroscopy (FT-IR), and the photocatalytic activity of $Zn_{1-x}Co_xMn_2O$ nanocrystals was evaluated by the photodegradation of MO dye in aqueous solution under UV light irradiation.

2. Material and Methods

2.1. Synthesis. A facile hydrothermal method was used to synthesize $Zn_{1-x}Co_xMn_2O_4$ ($x = 0$, 0.1, 0.3, and 0.5) nanocrystals. In a typical experiment, zinc nitrate ($Zn(NO_3)_2{\cdot}6H_2O$, AR, Tianjin Kaixin Chemical Industry Co. Ltd.), manganese nitrate ($Mn(NO_3)_2{\cdot}6H_2O$, AR, Tianjin Kemeiou Reagent Co. Ltd.), cobalt nitrate ($Co(NO_3)_2{\cdot}6H_2O$, AR, Shanghai Zhongqin Reagent Co. Ltd.), polyethylene glycol-400 (PEG-400, AR, Shandong West Asia Chemical Reagent Co. Ltd.), absolute ethyl alcohol (AR, China Pharmaceutical Group Reagent Co. Ltd), and citric acid (AR, Tianjin Kemeiou Reagent Co. Ltd.) were used in this study without any further purification. According to the chemical formula of $Zn_{1-x}Co_xMn_2O_4$ ($x = 0$, 0.1, 0.3, and 0.5) and the molar ratio of metal cations, the stoichiometric quantities of zinc nitrate, cobalt nitrate, and manganese nitrate as precursors were weighed. $Zn(NO_3)_2$, $Mn(NO_3)_2$, and $Co(NO_3)_2$ were mixed in distilled water and magnetically stirred at room temperature for 30 min. Meanwhile, appropriate amounts of citric acid and PEG-400 were dripped into the above-mixed solution under magnetic stirring for 3 hours. Subsequently, the resulting solution was transferred to a 100 mL Teflon-lined stainless steel autoclave. The hydrothermal reaction process was conducted at 180°C for 24 h in an oven and then cooled to room temperature naturally. Finally, the resultant precipitate was separated centrifugally, washed several times with distilled water and absolute alcohol, respectively, and then dried at 60°C in a vacuum oven for 10 h. Thus, $Zn_{1-x}Co_xMn_2O_4$ nanocrystals were collected and used for further study. By comparison, $Zn_{1-x}Co_xMn_2O_4$ nanoparticles with different ratios ($x = 0$, 0.1, 0.3, and 0.5) were also prepared using the abovementioned procedure.

2.2. Characterization. The crystal structure of the as-obtained samples was examined by X-ray diffractometer (XRD) using the CuKα source ($\lambda = 1.54056$ Å), the scanning rate 0.005°/s, and step size 0.02°. The morphology of the samples was investigated using a field emission scanning electron microscope (SEM) (JEOL JSM-6701F) equipped with an X-ray energy dispersive spectroscopy (XEDS). The ultraviolet-visible (UV-Vis) diffuse reflectance spectra (DRS) of the products were recorded on a UV-Vis spectrophotometer (PERSEE TU-1901) using BaSO4 as reference. Fourier transform infrared spectroscopy (FT-IR) studies were measured by a Nexus 670 FT-IR spectrometer in the range of 4000–400 cm^{-1}.

2.3. Photocatalytic Activity Test. The photocatalytic property of the samples was evaluated by measuring the degradation of methyl orange (MO) aqueous solution in a cylindrical glass vessel under simulated sunlight, and the reaction vessel was kept at a constant temperature using a circulating cooling system. The reaction solution was irradiated with the light source of a 300 W xenon lamp, and the distance between the solution surface and the light source was kept at 30 cm to avoid thermal effect. In this work, 20 mg of the as-synthesized samples was dispersed into a 100 mL MO aqueous solution (the initial MO aqueous solution concentration was 10 mg/L). The mixed suspensions were magnetically stirred for 30 min in the dark to reach the adsorption-desorption equilibrium between the photocatalyst and organic dye MO. During the photocatalytic process, about 2.5 mL of the reaction solution was collected from the container at predetermined intervals (30, 60, 90, 120, and 150 min) and the solid catalyst powder was separated and recovered by external magnetism field method. Then, the concentration of residual MO in the solution was determined by detecting the adsorption and degradation performance using an UV-visible spectrophotometer.

3. Results and Discussion

3.1. Structural Characterization. Figure 1 depicts the XRD patterns of pure $ZnMn_2O_4$ and Co-doped $Zn_{1-x}Co_xMn_2O_4$ samples. The diffraction peaks of all samples can be well indexed to single-phase $ZnMn_2O_4$ tetragonal structures (space group: I41/amd, $a = b = 0.5722$ nm, and $c = 0.9326$ nm), which are in agreement with the reported values of JCPDS card no. 71-2499 [24]. No extra diffraction peaks of other impurity phases such as metal oxides or metal clusters are detected when the doping atomic percentage ranges from 10% to 50% from the XRD patterns, indicating that all Co ions are assumed to be successfully incorporated into Zn^{2+} ion sites without changing the parent $ZnMn_2O_4$ structure. The crystallite size of the samples is calculated from the full width at half maximum (FWHM) and the peak position using the most intense diffraction peak (211) by the following Scherrer formula: $D = K\lambda/B\cos\theta$, where D represents the crystallite size, $K = 0.9$ is the Scherrer constant, λ is the wavelength of X-ray (CuKα, 1.54056 Å), θ is the Bragg diffraction angle, and B is FWHM in radians of the (211) plane. The crystallite sizes for $Zn_{1-x}Co_xMn_2O_4$ ($x = 0$, 0.1, 0.3, and 0.5) are 36, 33, 31, and 29 nm; it is clear that the crystallite size gradually decreases with the increase of the Co doping amount.

3.2. Morphological Studies. The SEM image of the pure $ZnMn_2O_4$ sample is showed in Figure 2(a). It is clearly visible that the morphology of pure $ZnMn_2O_4$ is a regular porous microsphere architecture mainly composed of many

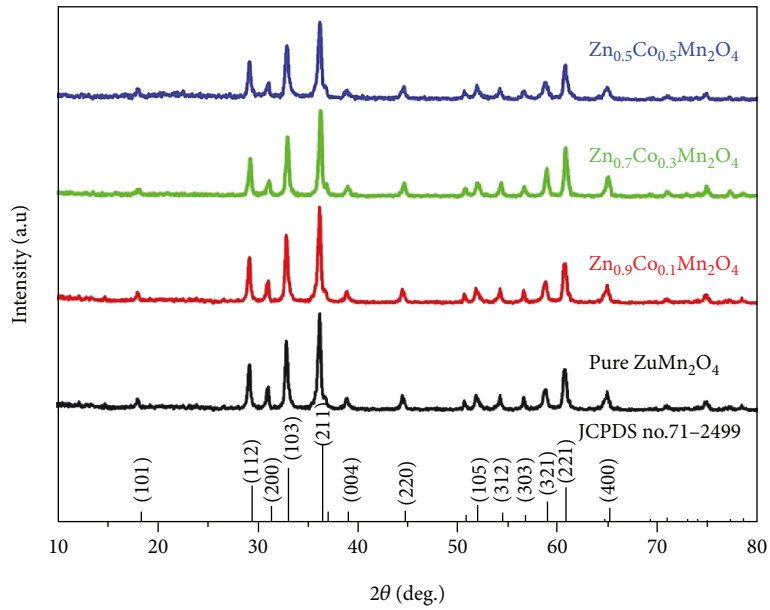

Figure 1: XRD patterns of $Zn_{1-x}Co_xMn_2O_4$ samples.

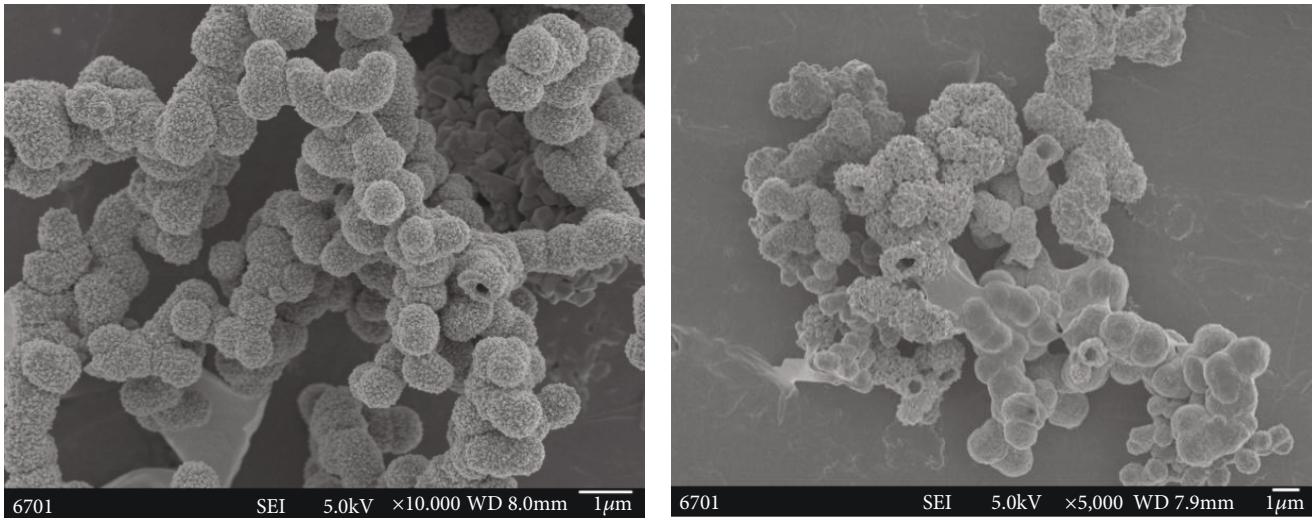

(a) (b)

Figure 2: SEM images of (a) pure $ZnMn_2O_4$ and (b) $Zn_{0.7}Co_{0.3}Mn_2O_4$ samples.

nanoparticles, with the diameter of the rough and porous microspheres ranging from 300 to 500 nm, with the average diameter of about 400 nm. Figure 2(b) presents the SEM image of the $Zn_{0.7}Co_{0.3}Mn_2O_4$ sample, showing a loose and irregular microsphere morphology composed of massive nanoparticles. With the increase of the Co doping content, the edges of the microsphere become looser and hollower and some stacked microspheres appear in breakage and exhibit hollow microspheres. The hollow microspheres grow bigger in size and rougher and irregular in morphology. This loose hollow microsphere structure contributes to improving the electrochemical performance.

Figure 3(a) shows the XEDS patterns of the pure $ZnMn_2O_4$ sample to further clarify the chemical components of the as-prepared samples. It is easily found that pure $ZnMn_2O_4$ mainly exhibits the peak characteristic of Zn, Mn, and O elements. Figure 3(b) obviously confirms the presence of Co elements besides Zn, Mn, and O elements for the $Zn_{0.7}Co_{0.3}Mn_2O_4$ sample, whereas the spectrum of pure $ZnMn_2O_4$ does not find the presence of Co elements. The XEDS results further verify XRD , which indicates that Co-doped $ZnMn_2O_4$ nanocrystals were successful synthesized by hydrothermal method and Co^{2+} is successfully substituted as dopant in the $ZnMn_2O_4$ matrix. It is evident

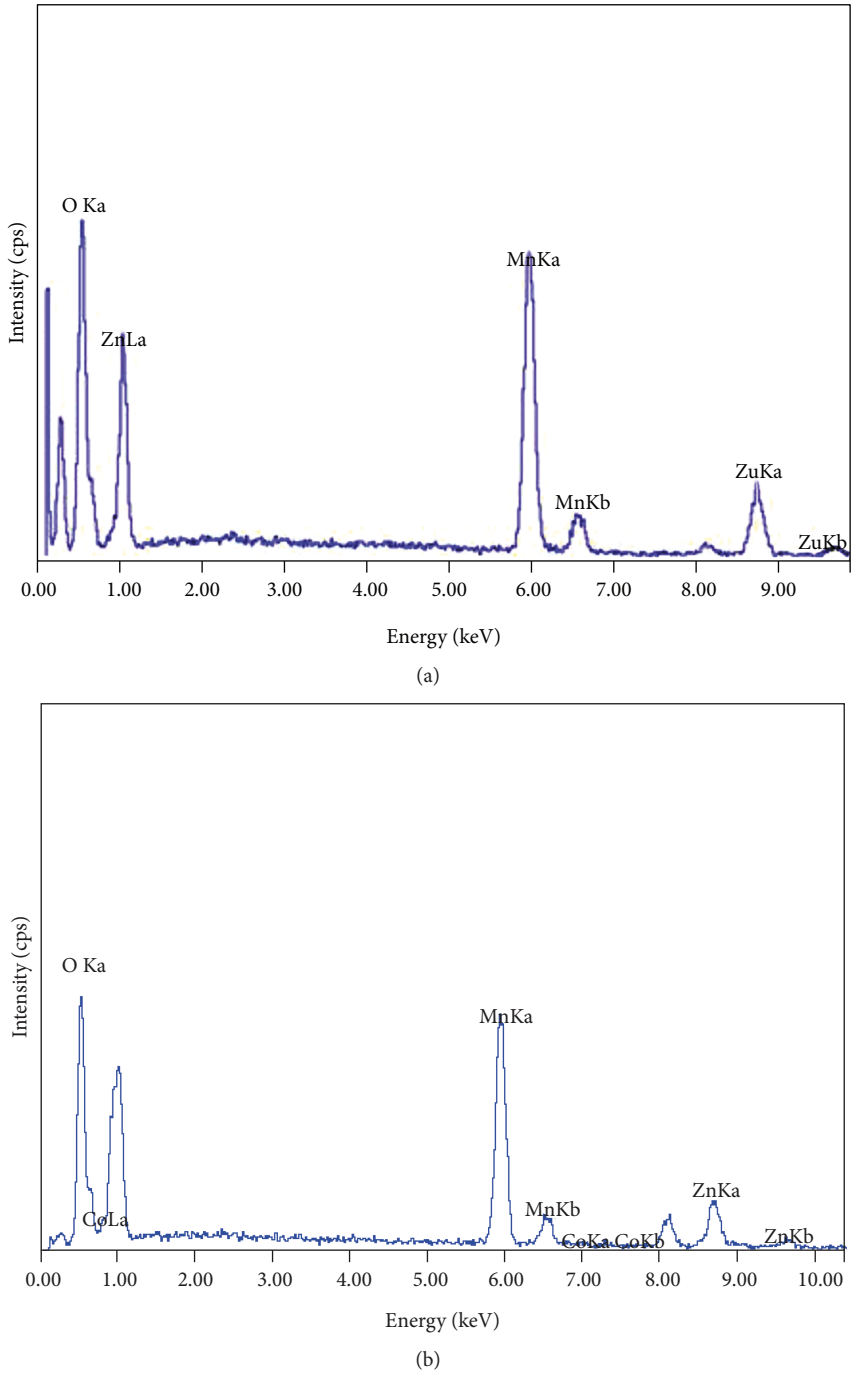

Figure 3: XEDS patterns of (a) pure $ZnMn_2O_4$ and (b) $Zn_{0.7}Co_{0.3}Mn_2O_4$ samples.

that the synthesize condition helps to further study the influence of Co doping concentration on the properties of $Zn_{1-x}Co_xMn_2O_4$ nanocrystals.

3.3. UV-Vis DRS Results. The optical properties of the samples are investigated by UV-Vis DRS. Figure 4(a) shows the absorption spectra of $Zn_{1-x}Co_xMn_2O_4$ samples. From Figure 4(a), Co-doped $Zn_{1-x}Co_xMn_2O_4$ samples show the similar absorption property as that of the pure $ZnMn_2O_4$ except that the absorption edge slightly shifts to a short wavelength with increasing Co content. The drift of the absorption edge revealed the interaction between Co ions and $ZnMn_2O_4$. For $Zn_{1-x}Co_xMn_2O_4$ nanocrystals with a direct band structure, according to the Tauc rule [25]: $[\alpha h\nu]^2 = A(h\nu - Eg)$, the optical band gap Eg is evaluated from the linear intercept of the $(ahv)^2$ versus hv plots as displayed in Figure 4(b). Consequently, the band gaps for $Zn_{1-x}Co_xMn_2O_4$ ($x = 0$, 0.1, 0.3, and 0.5) are calculated to be 2.21, 2.07, 2.02, and 1.98 eV, respectively. Furthermore, the band gap of the Co-doped $ZnMn_2O_4$ samples smaller than

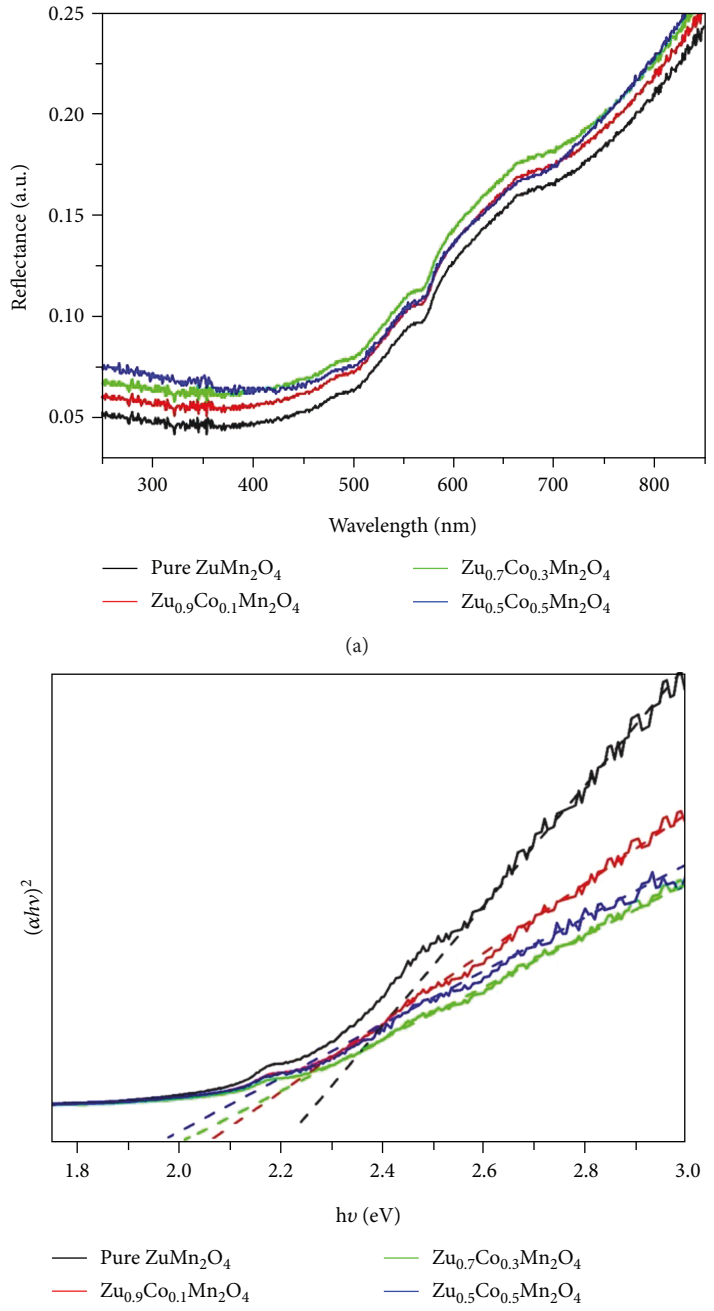

Figure 4: (a) UV-Vis diffuse reflectance spectra and (b) $(\alpha h\nu)^2$ versus $h\nu$ curves of $Zn_{1-x}Co_xMn_2O_4$ samples.

that of pure $ZnMn_2O_4$ and the band gap energy gradually decrease with the increase of Co concentration. This is manifested by the presence of a redshift in the band gap energy for Co-doped $Zn_{1-x}Co_xMn_2O_4$ nanocrystals.

3.4. FT-IR Spectra. The chemical structure of $Zn_{1-x}Co_xMn_2O_4$ samples was investigated using FT-IR, and the results were shown in Figure 5, wherein all of the samples exhibit very similar FT-IR absorption bands. A broad absorption band at 3410 cm^{-1} in the spectrum of $Zn_{1-x}Co_xMn_2O_4$ nanocrystals corresponds to O-H stretching vibrations of chemically bonded hydroxyl groups. The peak that appeared at 2923 cm^{-1} attributed to the vibrational absorption peaks corresponding to the C-H bonds [26], and the peak at 1542 cm^{-1} was caused by the C=O stretching vibrations of the remaining carbonyl groups in the compound [27]; the band at 1367 cm^{-1} can be assigned to the organic compounds of PEG-400 or alcohol induced in the process of preparation and test, and the presence of the peak at 1084 cm^{-1} is owing to C–O stretching vibrations [26]. It is noteworthy that two distinct peaks that appear at 505 and 622 cm^{-1} are dependent on the formation of metal–oxygen bonds of tetrahedral and

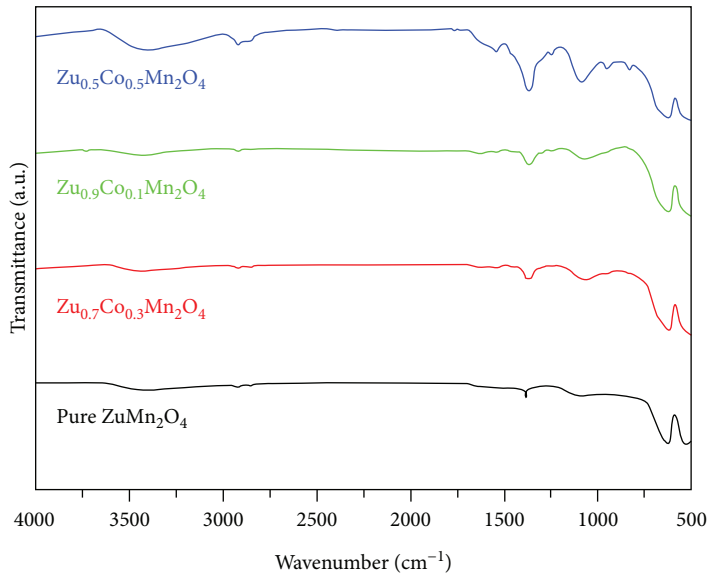

Figure 5: FT-IR spectra of $Zn_{1-x}Co_xMn_2O_4$ samples.

octahedral sites, i.e., Zn–O and Mn–O bonds [28]; these bands confirm the formation of spinel compounds for $Zn_{1-x}Co_xMn_2O_4$ nanocrystals. The corresponding peak position of the Fourier infrared spectrum of the sample did not change with the increase of the Co doping concentration, which is also consistent with the XRD data, indicating that Co^{2+} was successfully doped into the $ZnMn_2O_4$ lattice.

3.5. Photocatalytic Performance. In order to study the influence of Co doping concentration on the degradation efficiency, MO dye was selected as target pollutant for evaluating the photocatalytic activity of $Zn_{1-x}Co_xMn_2O_4$ nanocrystals. Figure 6(a) depicts the MO degradation of $Zn_{1-x}Co_xMn_2O_4$ samples with different doping ratios versus time (t) under simulated sunlight irradiation. Blank experiment was performed without any catalyst, it was found that there was no obvious self-degradation in the MO dye aqueous solution under visible light irradiation for 180 min, the blank experiment suggested that MO has good stability without catalyst, and the spontaneous photolysis can be negligible under visible light illumination. It is worth noting that the concentration of the MO dye slightly decreased when the reaction mixture is stirred for 30 min without light illumination, because $Zn_{1-x}Co_xMn_2O_4$ nanocrystals possess a larger specific surface area and can adsorb the MO dye well. The degradation rate of pure $ZnMn_2O_4$ is about 57% after xenon lamp irradiation for 150 mins, while the photocatalytic activity of $Zn_{1-x}Co_xMn_2O_4$ samples is obviously higher than that of pure $ZnMn_2O_4$ samples, and the decolorization rates are 69%, 75%, and 82%. It is obvious that the photocatalytic performance increases with the increase of Co doping amount and Co^{2+} ions replaced the lattice site of Zn^{2+} to generate single-phase $ZnMn_2O_4$ nanocrystal results in the effective separation of photoinduced electron-hole pairs to improve the photocatalytic activity.

To better compare the photocatalytic efficiency for $Zn_{1-x}Co_xMn_2O_4$ nanocrystals of MO decolorization, the kinetic study was performed using a first-order kinetic equation: $\ln(C_t/C_0) = k$, where k represents reaction rate constant (h^{-1}), t is the irradiation time, and C_t and C_0 denote the initial concentration and the reaction concentration, respectively, of MO after light irradiation. The first-order kinetics of $Zn_{1-x}Co_xMn_2O_4$ nanocrystals for photocatalytic decolorization of MO as shown in Figure 6(b) and the k values for $Zn_{1-x}Co_xMn_2O_4$ ($x = 0.1$, 0.3, and 0.5) are 0.470, 0.545, and 0.658 h^{-1}, respectively; these values demonstrate that doped $Zn_{1-x}Co_xMn_2O_4$ nanocrystals have a higher efficiency than that of pure samples ($k = 0.336$ h^{-1}). The improvement of photocatalytic efficiency is mainly due to the fact that Co-doped $Zn_{1-x}Co_xMn_2O_4$ nanocrystals possess smaller particle size and larger specific surface area and Co^{2+} can adjust the crystal structure and energy band structure, which accelerate the migration of the photogenerated electron-hole pairs toward its surface and prevent the electron-hole pairs from recombination.

The stability and reusability for the $Zn_{0.5}Co_{0.5}Mn_2O_4$ sample were evaluated by cyclic experiments of photocatalytic degradation of MO under the same conditions. As shown in Figure 7, the degradation efficiency of the $Zn_{0.5}Co_{0.5}Mn_2O_4$ sample exhibits a minor decrease from 82% to 79.5% after five consecutive cycles of photocatalytic experiments and the repetition rate is still maintained at 80%. The little decreases may relate to the particle aggregation of the sample after a long time reaction. Hence, $Zn_{1-x}Co_xMn_2O_4$ nanocrystals possess excellent photocatalytic active and good stability; these results demonstrate that Co-doped $ZnMn_2O_4$ nanocrystals possess good application prospects in photocatalytic degradation of pollutants.

Under simulated sunlight irradiation, the electrons (e^-) in the valence band (VB) of $ZnMn_2O_4$ can be excited to its

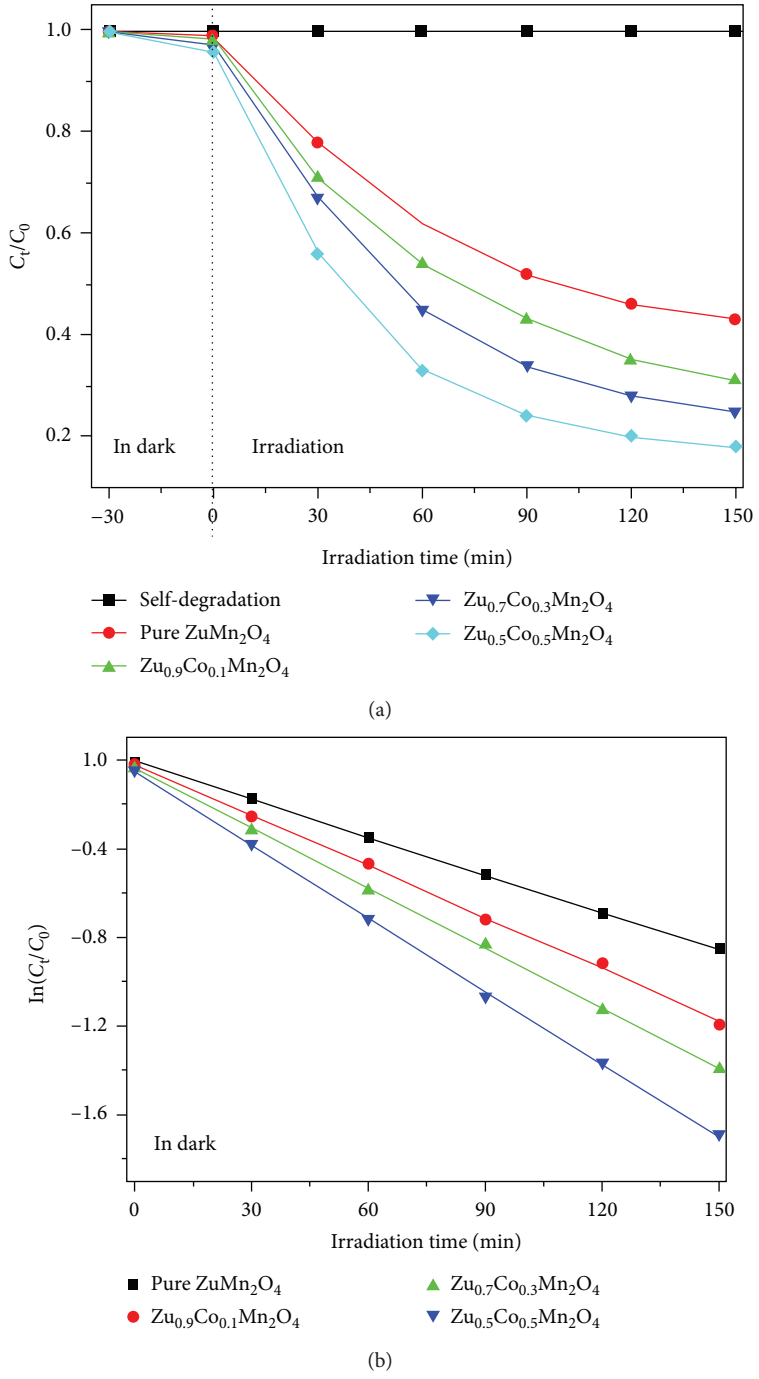

Figure 6: (a) Photocatalytic degradation of MO over time and (b) first-order kinetic curves of $Zn_{1-x}Co_xMn_2O_4$ samples.

conduction band (CB), while the holes (h^+) is generated in VB of $ZnMn_2O_4$. $Zn_{1-x}Co_xMn_2O_4$ nanocrystals can effectively promote the generation of photoinduced electron-hole pairs owing to the reduction of average grain size and the band gap for Co-doped $Zn_{1-x}Co_xMn_2O_4$ nanocrystals. The electrons at VB are excited to transition to CB, thus forming a hole in VB and generated an electron-hole pair (equation (1)). Electrons react with dissolved oxygen in the solution to form superoxide radicals ($^{\bullet}O^{2-}$). At the same time, photoinduced holes react with water to generate $^{\bullet}OH$, H^+ (equation (2)). Meanwhile, H^+ further reacts with oxygen to form H_2O_2 (equation (3)). Obviously, hydrogen peroxide reacts with O_2^- to produce $^{\bullet}OH$, OH^-, and O_2 (equation (4)). As strong oxidants, $^{\bullet}OH$ reacts strongly with organic pollutants and promote the decomposition of organic pollutants. Finally, $^{\bullet}OH$ and O_2^- oxidize MO to CO_2, H_2O, and other small molecule compounds (equation (5)) [3].

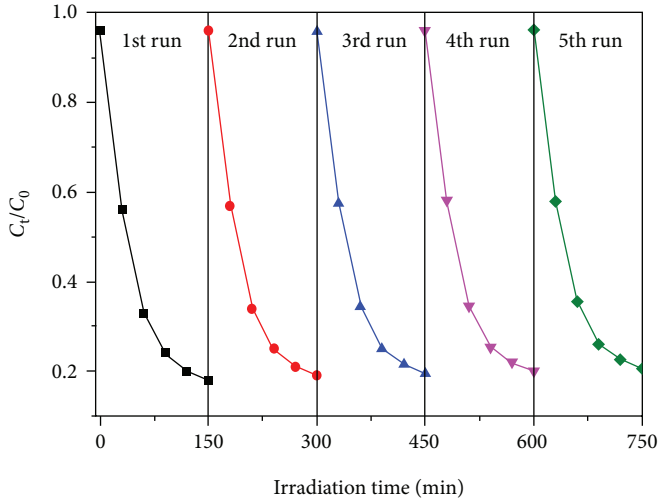

FIGURE 7: Photocatalytic cycle stability of $Zn_{0.7}Co_{0.3}Mn_2O_4$ samples.

Under simulated sunlight irradiation, the photocatalytic decolorization reaction of the photoinduced electron-hole transport for $Zn_{1-x}Co_xMn_2O_4$ nanocrystals is as follows [29]:

$$Zn_{1-x}Co_xMn_2O_4 + h\nu \longrightarrow Zn_{1-x}Co_xMn_2O_4(e^-) + Zn_{1-x}Co_xMn_2O_4(h^+), \quad (1)$$

$$Zn_{1-x}Co_xMn_2O_4(h^+) + H_2O \longrightarrow Zn_{1-x}Co_xMn_2O_4 + {}^{\bullet}OH + H^+,$$
$$Zn_{1-x}Co_xMn_2O_4(e^-) + O_2 \longrightarrow Zn_{1-x}Co_xMn_2O_4 + {}^{\bullet}O_2{}^-, \quad (2)$$

$$O_2 + H^+ \longrightarrow H_2O_2, \quad (3)$$

$$H_2O_2 + {}^{\bullet}O_2{}^- \longrightarrow {}^{\bullet}OH + OH^- + O_2, \quad (4)$$

$${}^{\bullet}OH, {}^{\bullet}O_2{}^- + \text{organic molecules} \longrightarrow H_2O + CO_2 + \text{mineral acids}. \quad (5)$$

4. Conclusion

(1) Co-doped $Zn_{1-x}Co_xMn_2O_4$ nanocrystals with different ratios ($x = 0$, 0.1, 0.3, and 0.5) were successfully synthesized via a facile hydrothermal method. All samples exhibit single-phase spinel tetragonal with good crystallization. Co^{2+} ions are successfully substituted for the lattice site of Zn^{2+} to generate single-phase $ZnMn_2O_4$ nanocrystals

(2) The morphologies of all the samples are loose hollow microsphere structures. The crystalline size decreases as Co-doped concentration increase. The energy band gap of Co-doped $Zn_{1-x}Co_xMn_2O_4$ nanocrystalline is smaller than that of pure $ZnMn_2O_4$ has been red shifted

(3) The photocatalytic activity of doped $Zn_{1-x}Co_xMn_2O_4$ samples is obviously higher than that of pure $ZnMn_2O_4$ samples for the photodegradation of MO under visible light irradiation. Co-doped $ZnMn_2O_4$ nanocrystals can act as a potential photocatalyst for photocatalytic degradation of the pollutants

Data Availability

The figure data used to support the findings of this study are included within the article.

Conflicts of Interest

The authors declare that they have no conflicts of interest.

Acknowledgments

This work was supported by the National Natural Science Foundation of China (no. 51261015) and the Natural Science Foundation of Gansu Province, China (no. 1308RJZA238).

References

[1] A. Fujishima, X. Zhang, and D. Tryk, "Heterogeneous photocatalysis: from water photolysis to applications in environmental cleanup," *International Journal of Hydrogen Energy*, vol. 32, no. 14, pp. 2664–2672, 2007.

[2] H. Zhai, J. Qi, X. Zhang et al., "Preparation and photocatalytic performance of hollow structure $LiNb_3O_8$ photocatalysts," *Nanoscale Research Letters*, vol. 12, no. 1, p. 519, 2017.

[3] W. Zhao, Z. Wei, L. Zhang, X. Wu, and X. Wang, "Cr doped SnS_2 nanoflowers: preparation, characterization and photocatalytic decolorization," *Materials Science in Semiconductor Processing*, vol. 88, pp. 173–180, 2018.

[4] K. Maeda and K. Domen, "New non-oxide photocatalysts designed for overall water splitting under visible light," *The Journal of Physical Chemistry C*, vol. 111, no. 22, pp. 7851–7861, 2007.

[5] C. Zheng, H. Yang, Z. Cui, H. Zhang, and X. Wang, "A novel $Bi_4Ti_3O_{12}/Ag_3PO_4$ heterojunction photocatalyst with enhanced photocatalytic performance," *Nanoscale Research Letters*, vol. 12, no. 1, p. 608, 2017.

[6] S. Thaweesak, M. Lyu, P. Peerakiatkhajohn et al., "Two-dimensional g-$C_3N_4/Ca_2Nb_2TaO_{10}$ nanosheet composites for efficient visible light photocatalytic hydrogen evolution," *Applied Catalysis B: Environmental*, vol. 202, pp. 184–190, 2017.

[7] F. Wang, H. Yang, H. Zhang, and J. Jiang, "Growth process and enhanced photocatalytic performance of $CuBi_2O_4$ hierarchical microcuboids decorated with AuAg alloy nanoparticles," *Journal of Materials Science: Materials in Electronics*, vol. 29, no. 2, pp. 1304–1316, 2018.

[8] Z. Li, J. Zhang, J. Lv, L. Lu, C. Liang, and K. Dai, "Sustainable synthesis of CeO_2/CdS-diethylenetriamine composites for enhanced photocatalytic hydrogen evolution under visible light," *Journal of Alloys and Compounds*, vol. 758, pp. 162–170, 2018.

[9] J. Zou, B. Liu, H. Liu, Y. Ding, T. Xin, and Y. Wang, "Facile synthesis of interconnected mesoporous $ZnMn_2O_4$ nanopeanuts for Li-storage via distinct structure design," *Materials Research Bulletin*, vol. 107, pp. 468–476, 2018.

[10] M. Abdollahifar, S.-S. Huang, Y.-H. Lin et al., "High-performance carbon-coated $ZnMn_2O_4$ nanocrystallite supercapacitors with tailored microstructures enabled by a novel solution combustion method," *Journal of Power Sources*, vol. 378, pp. 90–97, 2018.

[11] B. Ameri, S. S. H. Davarani, H. R. Moazami, and H. Darjazi, "Cathodic electrosynthesis of $ZnMn_2O_4/Mn_3O_4$ composite nanostructures for high performance supercapacitor applications," *Journal of Alloys and Compounds*, vol. 720, pp. 408–416, 2017.

[12] H. Wang, Z. Li, J. Xu, Y. Zhang, L. Yang, and W. Qiu, "Resistance switching properties of Ag/$ZnMn_2O_4$/p-Si fabricated by magnetron sputtering for resistance random access memory," *Journal of Wuhan University of Technology-Materials Science Edition*, vol. 30, no. 6, pp. 1159–1162, 2015.

[13] J. Morán-Lázaro, E. Guillen-López, F. López-Urias et al., "Synthesis of $ZnMn_2O_4$ nanoparticles by a microwave-assisted colloidal method and their evaluation as a gas sensor of propane and carbon monoxide," *Sensors*, vol. 18, no. 3, p. 701, 2018.

[14] L. Zhao, X. Li, and J. Zhao, "Fabrication, characterization and photocatalytic activity of cubic-like $ZnMn_2O_4$," *Applied Surface Science*, vol. 268, pp. 274–277, 2013.

[15] P. E. Saranya and S. Selladurai, "Efficient electrochemical performance of $ZnMn_2O_4$ nanoparticles with rGO nanosheets for electrodes in supercapacitor applications," *Journal of Materials Science: Materials in Electronics*, vol. 29, no. 4, pp. 3326–3339, 2018.

[16] X. Zhu, Z. Wei, W. Zhao, X. Zhang, L. Zhang, and X. Wang, "Microstructure and electrochemical properties of $ZnMn_2O_4$ nanopowder synthesized using different surfactants," *Journal of Electronic Materials*, vol. 47, no. 11, pp. 6428–6436, 2018.

[17] W. Zhou, D. Wang, L. Zhao et al., "Template-free fabrication of graphene-wrapped mesoporous $ZnMn_2O_4$ nanorings as anode materials for lithium-ion batteries," *Nanotechnology*, vol. 28, no. 24, article 245401, 2017.

[18] J. Bhagwan, N. Kumar, K. L. Yadav, and Y. Sharma, "Probing the electrical properties and energy storage performance of electrospun $ZnMn_2O_4$ nanofibers," *Solid State Ionics*, vol. 321, pp. 75–82, 2018.

[19] C. Wei, H. Wang, J. Xu, Y. Zhang, X. Zhang, and L. Yang, "Resistive switching behavior of Ag/$Mg_{0.2}Zn_{0.8}O$/$ZnMn_2O_4$/p^+-Si heterostructure devices for nonvolatile memory applications," *Journal of Wuhan University of Technology-Materials Science Edition*, vol. 32, no. 1, pp. 29–32, 2017.

[20] Q. Liu, Z. Zhang, B. Liu, and H. Xia, "Rare earth oxide doping and synthesis of spinel $ZnMn_2O_4$/KIT-1 with double gyroidal mesopores for desulfurization nature of hot coal gas," *Applied Catalysis B: Environmental*, vol. 237, pp. 855–865, 2018.

[21] R. Gherbi, Y. Bessekhouad, and M. Trari, "Optical and transport properties of Sn-doped $ZnMn_2O_4$ prepared by sol–gel method," *Journal of Physics and Chemistry of Solids*, vol. 89, pp. 69–77, 2016.

[22] W. H. Zhao, Z. Q. Wei, X. L. Zhu, X. D. Zhang, and J. L. Jiang, "Optical and magnetic properties of diluted magnetic semiconductor $Zn_{0.95}M_{0.05}S$ nanorods prepared by a hydrothermal method," *International Journal of Materials Research*, vol. 109, no. 5, pp. 405–412, 2018.

[23] R. Gherbi, Y. Bessekhouad, and M. Trari, "Structure, optical and transport properties of Mg-doped $ZnMn_2O_4$," *Journal of Alloys and Compounds*, vol. 655, pp. 188–197, 2016.

[24] C. Feng, W. Wang, X. Chen, S. Wang, and Z. Guo, "Synthesis and electrochemical properties of $ZnMn_2O_4$ anode for lithium-ion batteries," *Electrochimica Acta*, vol. 178, pp. 847–855, 2015.

[25] Y. Yan, H. Yang, X. Zhao, R. Li, and X. Wang, "Enhanced photocatalytic activity of surface disorder-engineered $CaTiO_3$," *Materials Research Bulletin*, vol. 105, pp. 286–290, 2018.

[26] C. P. Neto, J. Rocha, A. Gil et al., "^{13}C solid-state nuclear magnetic resonance and Fourier transform infrared studies of the thermal decomposition of cork," *Solid State Nuclear Magnetic Resonance*, vol. 4, no. 3, pp. 143–151, 1995.

[27] Y. S. Feng, S. M. Zhou, Y. Li, C. C. Li, and L. D. Zhang, "Synthesis and characterization of tin oxide nanoparticles dispersed in monolithic mesoporous silica," *Solid State Sciences*, vol. 5, no. 5, pp. 729–733, 2003.

[28] S. Naz, S. K. Durrani, M. Mehmood, and M. Nadeem, "Hydrothermal synthesis, structural and impedance studies of nanocrystalline zinc chromite spinel oxide material," *Journal of Saudi Chemical Society*, vol. 20, no. 5, pp. 585–593, 2016.

[29] F. Achouri, S. Corbel, L. Balan et al., "Porous Mn-doped ZnO nanoparticles for enhanced solar and visible light photocatalysis," *Materials & Design*, vol. 101, pp. 309–316, 2016.